Enhanced Stimulated Brillouin Scattering in Unsuspended Silicon Waveguide Assisted with Genetic Algorithms

PENG LI,[1] SHUMENG WANG,[1] GORAN Z. MASHANOVICH[2] JUN-YU OU,[2] AND JIZE YAN[1,*]

[1] *School of Electronics and Computer Science, University of Southampton,Southampton SO17 1BJ, United Kingdom*
[2] *Optoelectronics Research Centre, University of Southampton,Southampton SO17 1BJ, United Kingdom*
[*] *J.Yan@soton.ac.uk*

Abstract: Stimulated Brillouin scattering (SBS), originating from the coupling between optical and acoustic waves, has been widely applied in many fields. Silicon is the most used and important material in micro-electromechanical systems (MEMS) and integrated photonic circuits. However, strong acoustic-optic interaction in silicon requires mechanical release of the silicon core waveguide to avoid acoustic energy leakage into the substrate. This will not only reduce the mechanical stability and thermal conduction, but also increase the difficulties for fabrication and large-area device integration. In this paper, we propose a silicon-aluminium nitride(AlN)-sapphire platform for realizing large SBS gain without suspending the waveguide. AlN is used as a buffer layer to reduce the phonon leakage. This platform can be fabricated via the wafer bonding between silicon and commercial AlN-sapphire wafer. We adopt a full-vectorial model to simulate the SBS gain. Both the material loss and the anchor loss of the silicon are considered. We also apply the genetic algorithm to optimize the waveguide structure. By limiting the maximum etching step number to two, we obtain a simple structure to achieve the SBS gain of 2462 $W^{-1}m^{-1}$ for forward SBS, which is 8 times larger than the recently reported result in unsuspended silicon waveguide. Our platform can enable Brillouin-related phenomena in centimetre-scale waveguides. Our findings could pave the way toward large-area unreleased opto-mechanics on silicon.

1. Introduction

Stimulated Brillouin scattering (SBS), arising from the coupling between optical and acoustic waves, is a third-order nonlinear effect [1, 2]. It is recently predicted that in nanoscale waveguide, the increased radiation pressure due to the strong confinement of optical mode can lead to new forms of SBS nonlinearity in short length [3]. Since then, many different materials have been investigated to generate high SBS gain in integrated photonic circuits, such as chalcogenide glass [4, 5], silicon [6–8], silicon nitride [9, 10], AlGaAs [11] and GeSbS [12].

Among them, silicon has drawn the most attention due to its wide applications in MEMS and integrated photonic circuits [13]. However, a strong SBS interaction needs the simultaneous confinement of optical and acoustic waves [14], which requires a full or partial suspension of the silicon core waveguide [15]. This will result in reduced mechanical robustness, limited thermal conduction, complicated fabrication thus hindering the integration of large-area optomechanical devices on a single chip. Therefore, a silicon-compatible platform displaying large Brillouin gain while simultaneously not requiring the release of the silicon core, is desired.

Recently, a silicon-silicon nitride (Si_3N_4)-silica platform has been proposed to realize SBS without suspending the core waveguide [16]. However, this platform has several limitations: The first problem is the difficulty in growing high quality Si_3N_4. Current deposition methods cannot

grow single crystalline Si_3N_4on top og silica due to the lattice mismatch [17]. However, the mechanical properties of Si_3N_4 depend on its crystal quality and orientation [18], leading to the unpredictability in the final device performance.

The second issue is that the SBS gain coefficient in unsuspended structure is greatly reduced. This results from the fact that the moving boundaries contribution is largely decreased due to the fixed boundary. To the best of our knowledge, the best result in non-suspended design is only around 300 $W^{-1}m^{-1}$ [16], while in suspended Si waveguide, the result is 10 times larger [6].

Aluminium nitride (AlN) is another material that can be used for realizing sufficient SBS in non-suspension silicon waveguide [19]. AlN has a lower refractive index and higher acoustic velocities than these of silicon [20, 21]. As a result, AlN can be used as a buffer layer to avoid the phonon leakage, while strongly confining the optical wave at the same time [22]. In addition, direct wafer bonding between silicon and AlN has recently been reported [23], which guaranteed the crystal qualities of both silicon and AlN.

In this paper, we propose Si-AlN-Sapphire platform for realizing large SBS gain without suspending the Si waveguide. A full-vectorial model is applied to calculate the SBS gain coefficient. The material loss and anchor loss are calculated in the model. We leverage the genetic algorithm to optimize the waveguide structure so that the SBS gain coefficient can be maximized. Besides, by limiting the maximum etching step to two, a simple and fabricable non-suspended structure is obtained. The best gain coefficient comes from the forward SBS of fundamental TE-like mode with the value of 2462 $W^{-1}m^{-1}$. This gain value is 8 times larger than the recent result [16]. Our platform can enable Brillouin-related phenomena in centimetre-scale waveguide. Our findings could pave the way toward large-area unreleased opto-mechanics on silicon.

2. Principle

2.1. Full-vectorial model for calculating SBS gain coefficient

In this work, we use the full-vectorial model from [24] to calculate the SBS gain via photoelastic effect and moving boundary. Assuming the light is propagating along a translationally invariant waveguide (y-axis in this paper), then the optical pump and Stokes waves can be approximately described as modulated optical eigenmode, with electric field distributions:

$$\mathbf{E_p}(r,t) = a_p(y,t)\cdot\widetilde{\mathbf{e_p}}(x,z)\cdot e^{i(\mathbf{k_p}\cdot y-\omega_p\cdot t)} + c.c. \tag{1}$$

$$\mathbf{E_s}(r,t) = a_s(y,t)\cdot\widetilde{\mathbf{e_s}}(x,z)\cdot e^{i(\mathbf{k_s}\cdot y-\omega_s\cdot t)} + c.c. \tag{2}$$

where $a_i(y,t)$ (with i=p,s) is the slowly-varying envelope function of the pump and Stokes waves, respectively. And $\widetilde{\mathbf{e_i}}(x,z)$ represent the spatial mode distribution, which are the solutions of the Helmholtz equations with wave vector $\mathbf{k_i}$ and angular frequency ω_i. Note that following [24], the energy in each mode is not normalized, instead the energy terms are carried through to the gain calculation in Eq. (7).

Similarly, the acoustic mode can also be written as :

$$\mathbf{U} = b(y,t)\widetilde{\mathbf{u}}(x,z)e^{j(\mathbf{q}\cdot y-\Omega_B\cdot t)} + c.c. \tag{3}$$

where $b(y,t)$, $\mathbf{q}$ and Ω_B are the slowly varying envelope function, the wave vector and the angular frequency of the acoustic wave. The function $\widetilde{\mathbf{u}}(x,z)$ is the spatial distribution of the acoustic wave displacement, which is the solution of the following eigenvalue problem:

$$\rho\Omega_B^2\widetilde{u_i} + \sum_{ijkl}(\nabla_T + iq\hat{\mathbf{y}})_j c_{ijkl}(\nabla_T + iq\hat{\mathbf{y}})_k\widetilde{u_l} = 0. \tag{4}$$

where i,j,k,l=(x,y,z), ρ and c_{ijkl} are the material density and the elastic tensor, respectively. The acoustic wave decay can be determined by the dynamic viscosity η of the waveguide material [25], this term will be considered as the material loss in this paper.

In a nano-scale waveguide, two mechanisms will contribute to the final SBS gain, which are the photoelastic interaction Q_{PE} and the moving boundary Q_{MB} (units: W$\cdot$ m^{-1} $\cdot$ s):

$$Q_{PE} = \varepsilon_0 \varepsilon_{core}^2 \int dr^2 \sum_{ijkl} e_i^{(s)*} e_j^{(p)} p_{ijkl} \partial_k \widetilde{u}_l^*. \tag{5}$$

$$\begin{aligned} Q_{MB} = \int_C dr (\hat{\mathbf{n}} \cdot \widetilde{\mathbf{u}}^*)[\varepsilon_0(\varepsilon_{core} - \varepsilon_{clad})(\widetilde{\mathbf{e}}_s \times \hat{\mathbf{n}})^* \cdot (\widetilde{\mathbf{e}}_p \times \hat{\mathbf{n}}) \\ -\varepsilon_0^{-1}(\varepsilon_{core}^{-1} - \varepsilon_{clad}^{-1})(\widetilde{\mathbf{d}}_s \cdot \hat{\mathbf{n}})^* \cdot (\widetilde{\mathbf{d}}_p \cdot \hat{\mathbf{n}})]. \end{aligned} \tag{6}$$

where ε_i (i=0,core,clad) are the permittivity for vacuum, core material and cladding material, respectively, and $\widetilde{\mathbf{d}}_i$ is the induction field. Eq. (5) is integrated over the whole transversal plane of the waveguide, while Eq. (6) is a line integral to be carried out along the waveguide boundaries with normal vector $\hat{\mathbf{n}}$ pointing from the core material to the cladding material.

Finally, the total Brillouin gain can be calculated by means of:

$$G_0 = Q_m \cdot \frac{2\omega_p \left| Q_{PE} + Q_{MB} \right|^2}{P_p P_s \varepsilon_B}. \tag{7}$$

where Q_m, P_p, P_s and ε_B are the mechanical quality factor, the pump, Stokes modal power (units: W) and acoustic modal energy (units: J $\cdot$ m $^{-1}$).

An efficient SBS interaction will only occur when the simultaneous conservations of energy and momentum [3] are satisfied.

$$\Omega_B = \omega_{\mathbf{p}} - \omega_{\mathbf{s}}. \tag{8}$$

$$\mathbf{q} = \mathbf{k_p} - \mathbf{k_s}. \tag{9}$$

According to the relative direction between pump and Stokes waves, SBS can be categorized either as forward SBS (FSBS), where pump and Stokes waves travel co-directionally, or as backward SBS (BSBS), where pump and Stokes waves travel counter-directionally.

Based on the fact that $\Omega_B \ll \omega_p, \omega_s$ and $\omega_p \approx \omega_s$ [14], q is almost zero for FSBS while $q \approx 2k_p$ for BSBS. In this paper, we focus on FSBS as it requires far fewer simulation steps than backward SBS, where phase matching requires simulation of several mechanical propagation vectors [26]. Apart from the above requirements, the field distribution of the selected acoustic mode also needs to match the optical mode distribution [27].

To better analyse the factors affecting the final gain coefficient, one can divide the right part of Eq. (7) into two parts. The first part is the mechanical quality factor Q_m. This parameter reflects the mechanical energy loss. The more phonon energy leaks into the substrate, the smaller the Q_m will be. There are various sources leading to the decrease in Q_m [28, 29]. The two main losses concerned here are material loss $Q_{material}$ and anchor loss Q_{anchor} [3, 30].

Material loss is the loss related to the acoustic wave frequency. Normally the higher the frequency, the more significant the material loss [31]. For silicon, in the frequency range of gigahertz, material loss is believed to be the main factor limiting mechanical Q factor to around 1000 [3, 16]. Material loss can also be calculated via the viscosity tensor of the material [6]. Table 1 summarizes the optical and mechanical properties of all the materials used in our model [20, 21, 32–39]. The crystal structure of silicon is cubic, while AlN and sapphire have the wurtzite crystal structure.

The working wavelength used for simulation in this paper is 1550 nm. At this wavelength Si has a higher refractive index than that of AlN, so the optical mode can be well confined in Si via internal reflection. Meanwhile the acoustic velocity of Si is smaller than that of AlN, so AlN can work as a buffer layer to prevent acoustic leakage into the substrate. The authors added

the viscosity tensor of silicon into the simulation model so that the actual material loss can be simulated [39].

It also needs to be highlighted that the waveguide in this paper is designed to be along the <110> crystal orientation of the silicon, which is rotated by $\pi/4$ from the <100> direction (the direction that the data is measured in [39]). This is because the SBS gain is predicted to be higher in this direction [25]. The detailed transformation of the tensor can be found in [19, 40].

Table 1. The material parameters used for the investigation of Brillouin gain: the refractive index n, density ρ and elastic tensor values c_{ij} are taken from [20, 21, 32–35]. The values for transverse and longitudinal velocities are calculated based on the density ρ and elastic tensor c_{ij}. The photoelastic tensor values are taken from [36–38]. The viscosity tensor values are taken from [39].

quantity	unit	Si[110](cubic)	AlN[001](Wurtzite)	Sapphire[001](Wurtzite)
n	–	3.47	2.02	1.74
ρ	kg/m^3	2329	3230	3980
c_{11}	GPa	194	410	497.6
c_{12}	GPa	35.2	149	162.6
c_{13}	GPa	63.9	99	117.2
c_{33}	GPa	166	389	501.8
c_{44}	GPa	79.6	125	147.2
c_{66}	GPa	51.05	130.5	167.5
v_t	m/s	9128	11270	11181
v_l	m/s	5846	6220	6082
p_{11}	–	-0.0895	-0.1	-0.23
p_{12}	–	0.0125	-0.027	-0.03
p_{13}	–	0.017	-0.019	0.02
p_{33}	–	-0.094	-0.107	-0.2
p_{44}	–	-0.051	-0.032	-0.1
p_{66}	–	-0.0555	-0.037	-0.1
η_{11}	mPa·s	6.15	–	–
η_{12}	mPa·s	4.91	–	–
η_{13}	mPa·s	5.16	–	–
η_{33}	mPa·s	5.90	–	–
η_{44}	mPa·s	0.62	–	–
η_{66}	mPa·s	0.37	–	–

As for the anchor loss Q_{anchor}, this can be numerically simulated by applying a perfectly matched layer (PML) [41] around the substrate. In the following section, the Q_m is the summation

of these two sources ($Q_m^{-1} = Q_{material}^{-1} + Q_{anchor}^{-1}$).

The accuracy of this full-vectorial method is validated by matching the simulation results with the measured results from [6]. The details concerning the validation of the model can be found in the authors' previously published paper [19].

One critical limitation of the unsuspended structure is the reduced Brillouin gain coefficient due to the sacrifice of the contribution from the moving boundary effect. Genetic algorithm (GA) has been used to develop novel structures for giant SBS gain coefficient [26]. However, most designs require complex fabrication processes, making them almost impossible to be fabricated.

In this paper, we apply the GA to optimize the core silicon waveguide structure to maximize the SBS gain coefficient. We limit the maximum etching step number to two so that the optimal structure is not too complicated to be fabricated. In the next section, the fundamental theory and the implementation of the GA will be introduced.

2.2. Genetic Algorithm

A typical GA can be divided into five stages: initial population, fitness function, selection, crossover and mutation [26, 42, 43]. Our initial population consists of 100 random samples. The optimization area is limited within the silicon layer with an area of 1 μm x 1 μm to reduce the computational time. The maximum etching step number is limited to two.

Next, we discretize each sample into a series of 50 nm x 50 nm squares with the properties corresponding to the material of that part. There are two reasons for this rasterized method: first, 50 nm is possible to the lithographically pattern; second this method allows us to keep the same mesh for all mutated samples [26]. Via this method, we are able to change the structure design without affecting boundary conditions for both optical and acoustical waves [26].

Each sample is decided by an array with eight parameters. These parameters are: waveguide width W, waveguide height H, number of first etching $\#EP1$, number of second etching $\#EP2$, the first etching position $EP1$, the second etching position $EP2$, etch depth for first etching $ED1$, and etch depth for second etching $ED2$,. Fig. 1 illustrates the process of generating one random initial population. The detailed parameters used for GA in this paper are summarized in Table 2.

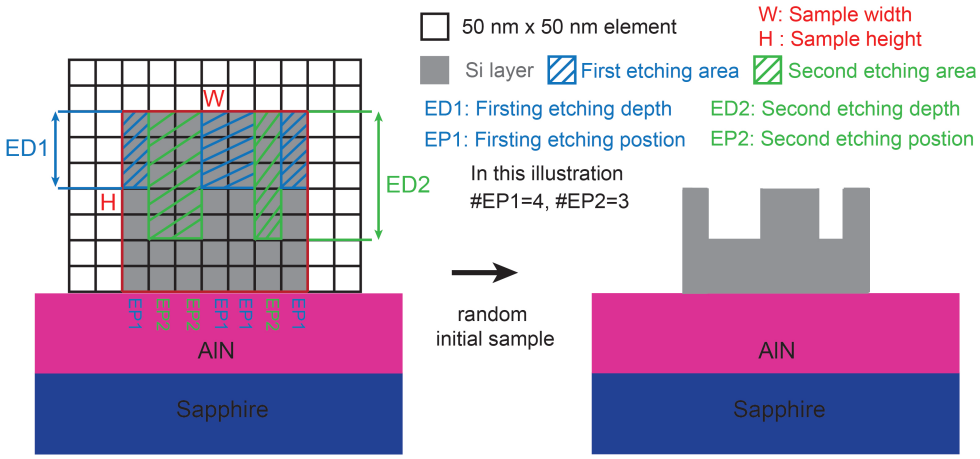

Fig. 1. The schematic illustration of generating an initial random sample: a total simulation area of 1 μm x 1 μm is discretized into a series of 50 nm x 50 nm squares. The simulation area is limited within silicon layer. Each sample is decided by eight parameters: waveguide width W, waveguide height H, first etching position $EP1$, second etching position $EP2$, etch depth for first etching $ED1$, etch depth for second etching $ED2$, number of first etching $\#EP1$ and number of second etching $\#EP2$.

Table 2. The parameters used for genetic algorithm in this paper

Optimization space	1 μm x 1 μm
Element area	50 nm x 50 nm
FEM mesh	Triangular
FEM mesh resolution	15 nodes per element
Number of EP1 $\#EP1$	Randomly select from (1:N), N=W/50 nm
Number of EP2 $\#EP2$	N-$\#EP1$
First etching position $EP1$	Randomly select number of $\#EP1$ positions from (1:N)
Second etching position $EP2$	The rest positions after $EP1$
First etching depth $ED1$	Randomly select from (50 nm:50 nm: H)
Second etching depth $ED2$	Randomly select from (50 nm:50 nm: H)
Initial size of population	100
Size of selection	50
Probability of mirror mutation (%)	20
Probability of reassign mutation (%)	20

A set of optical and mechanical modes is first calculated by COMSOL and these data are exported to calculate the SBS gain for each mode pair via Eq. (7) in Matlab. Q_m used in Eq. (7) are based on the material loss calculated with the viscosity from Table. 1 and anchor loss simulated via PML in COMSOL.The gain coefficient is used as the fitness score. The selection method is elitist, which means the samples with the highest gain (top 50) are selected for the next iteration [26]. However, all results are saved no matter whether they are selected or not.

After the selection, the crossover phase will happen where new samples are generated until the population is as large as the initial population. As shown in Fig. 2, to generate a new pair of samples (children α and β), two parent samples (Parent A and B) with their individual unique parameters are randomly chosen from the selected samples. During the crossover, the width and height of the parents will be swapped, generating two new combinations ($W1$ $H2$ and $W2$ $H1$). However, the remaining parameters will automatically follow the change of width and height. For example, the etching depth $ED1$ and $ED2$ will follow the swap of $H1$ and $H2$, the etching position and etching number will follow the swap of the width. As shown in Fig. 2, Children α is generated with Parent A's width and Parent B's height. Therefore, the etching position and etching numbers are taken from parent A and etching depth is taken from Parent B.

After the crossover stage, there is a certain mutation possibility for new generated samplers. The mutation phase in this work includes two mechanisms. one mechanism is called mirrored mutation, as shown in Fig. 3 (a). The original sample is mirrored across a randomly located axis. Then two new mutated samples are generated. One is mirrored from the right side of the axis and the other one from the left side of the axis. This mutation benefits symmetric waveguides.

The other mechanism is parameter re-assignation, as shown in Fig. 3 (b), one of the eight parameters will have the probability of being randomly re-assigned. If the re-assigned parameter is one of the etching-related parameters, no other parameter will be changed. However, if the mutated parameter is the waveguide height or width, similar to the crossover stage, the parameters related with W or H will also mutate. For example, if the waveguide width is changed, then the etching numbers and positions will also be modified accordingly.

Afterwards, the new population is then re-evaluated to calculate the SBS gain, the best samples are selected for the next generation, and the loop continues. When there is no further change in the sample with the highest gain coefficient, the algorithm will stop. Details of the GA code are not shown here for the sake of simplicity but it could be found in Supplement 1 section 1.

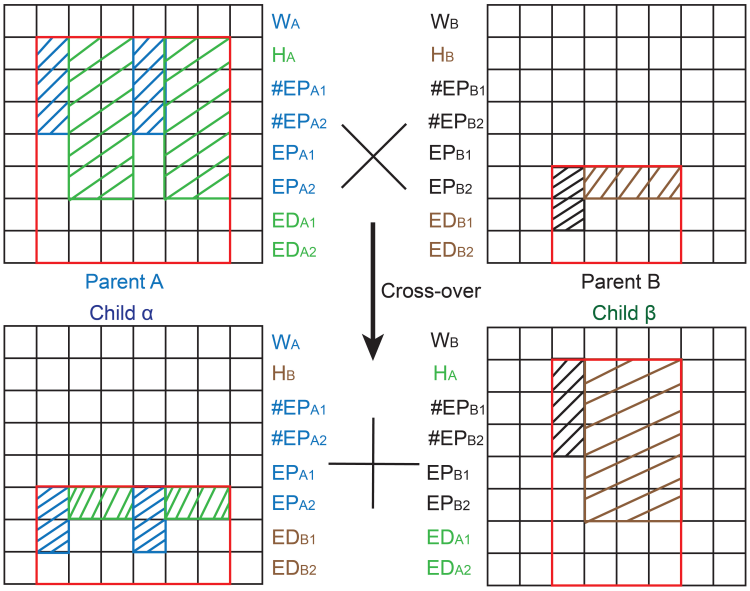

Fig. 2. The schematic illustration of the crossover stage: the width and height of the parents will be swapped, generating two new children. However, the etching depth $ED1$ and $ED2$ will follow the swap of $H1$ and $H2$, the etching position $EP1$ $EP2$ and etching number $\#EP1$ $\#EP2$ will follow the swap of the width.

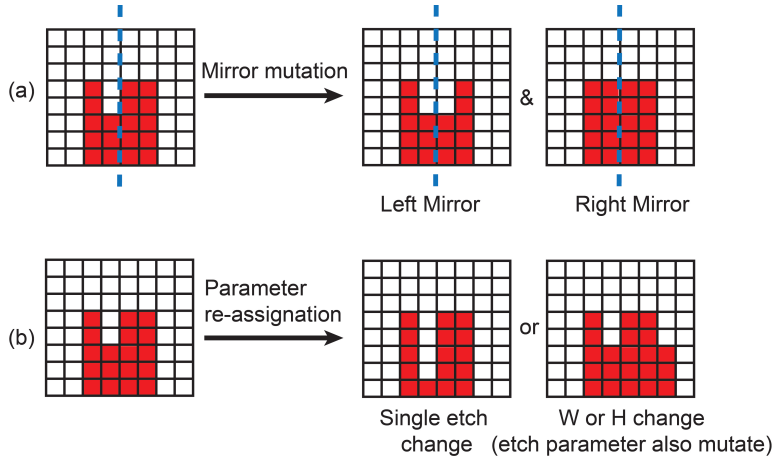

Fig. 3. The illustration of two mutation mechanisms: (a) is the mirror mutation. where the original sample is mirrored across a randomly located axis. Two new mutated samples are generated. (b) is the parameter re-assignation, where one parameter will be randomly reassigned. However, if the mutated parameter is the waveguide height or width, similar to the crossover stage, the related parameters will also mutate.

3. Results and discussions

3.1. Optimized waveguide structure for realizing large gain coefficient

Fig. 4 (a) shows the structure of the final optimized silicon waveguide. It is a thin and tall silicon waveguide with a shallow trench etched in the middle. The total thickness T of the waveguide is 620 nm, and the width W is 300 nm. The width a and height b of the trench is 100 nm and 105 nm, respectively. In this model, the thickness of AlN and sapphire are 600 nm and 700 nm, respectively. These values are the typical values from the commercial AlN wafer [44]. PML is designed to be 600 nm, which is thick enough to absorb the evanescent acoustic wave [45].

The fundamental TE-like and TM-like modes are shown in Fig. 4 (b) and (c). It can be seen that TM-like mode is better confined within the silicon waveguide, while TE-like mode has a stronger intensity on the boundary, which can be beneficial for increasing the SBS gain. Fig. 4 (d) shows the horizontal component of the selected acoustic mode. There is little energy leaking into the substrate, indicating strong confinement of the acoustic wave. In addition, the acoustic wave distribution matches with the TE-like mode optical mode distribution. Thus, it is expected that there is a strong coupling between the TE-like mode and the selected acoustic mode [27].

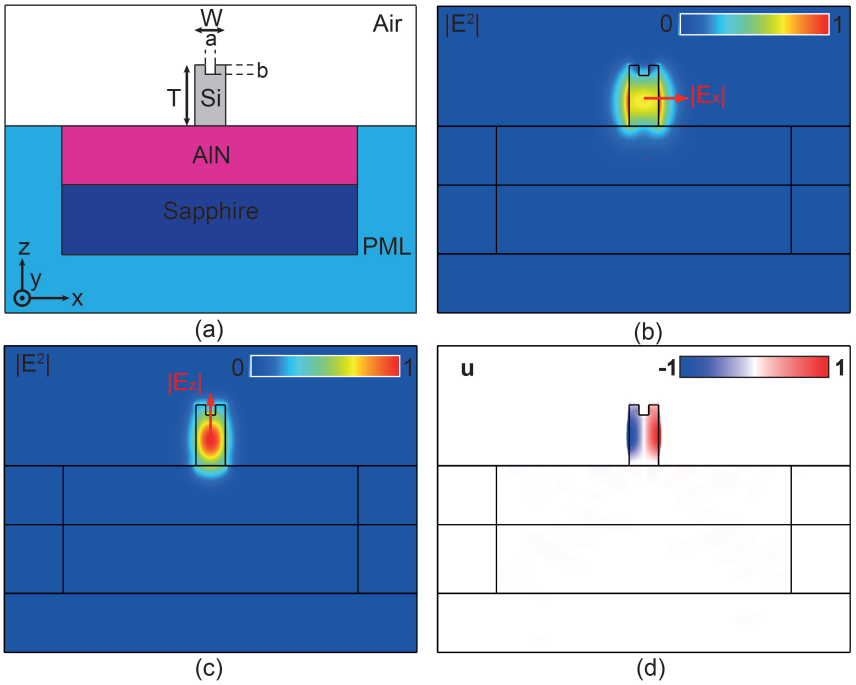

Fig. 4. The schematic illustration of Si-AlN-Sapphire platform: (a) The cross-section of the optimized waveguide structure, the total thickness of silicon waveguide T is 620 nm, width W is 300 nm. The trench is located at the centre of the silicon waveguide. The dimensions of the trench is that width a = 100 nm, and etch depth b = 105 nm. (b) and (c) show the computed normalized E_x and E_z components of the optical TE-like and TM-like modes. (d) is the horizontal component of the selected acoustic mode.

The best result we obtained is for the TE-like mode, when the total Brillouin gain coefficient is 2462 $\mathrm{W^{-1}m^{-1}}$ with Q_m of 323. This quality factor has reached the measured quality factor limited by the material loss [6]. For TM-like mode, the highest gain is only around 200 $\mathrm{W^{-1}m^{-1}}$ due to the mismatch of field distributions. Our result is 8 times larger than the recently reported result in unsuspended silicon waveguide [16].

3.2. *Influence of trench depth and width*

Although the structure is found by the algorithm, the authors investigated the influences of trench depth and width to see how the additional trench improves the gain coefficient.

First, we study the influence of the trench depth. From Eq. (7), it can be seen that the final gain coefficient is decided by mechanical quality factor Q_m and normalized gain coefficient g_0. As shown in Fig. 5 (a) and (b), with the change of etch depth, the normalized gain coefficient g_0 does not change dramatically for TE-like mode. While for TM-like mode, although g_0 has the tendency to grow, it remains under 1 $W^{-1}m^{-1}$ due to the field distributions mismatch. Besides, the moving boundary term is the main contribution for TE-like mode because of the higher optical intensity on the boundary. While for the TM-like mode, photoelastic effect becomes more dominant due to better confinement of the optical mode.

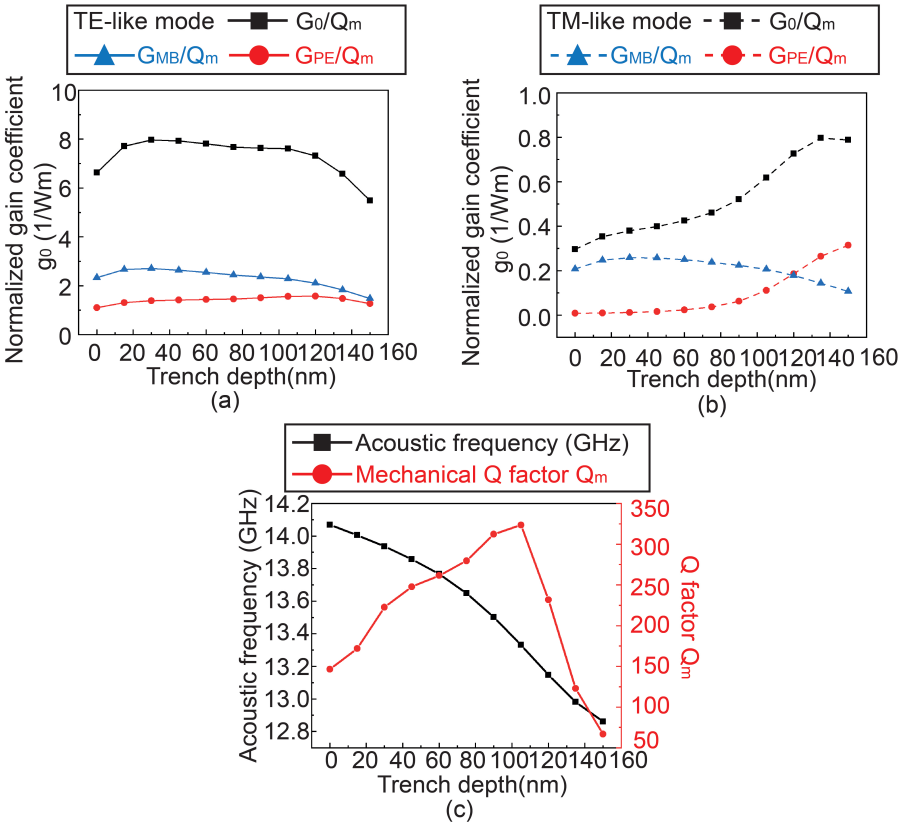

Fig. 5. The results of intramodal FSBS for TE-like and TM-like modes: (a) shows the variation of the normalized gain coefficient g_0 for TE-like mode against the trench depth. there is no obvious boost for g_0. (b) shows the g_0 for TM-like mode. Although it has the tendency to grow with deeper trench depth, overall g_0 remains under 1 $W^{-1}m^{-1}$ due to the field distributions mismatch. (c) The acoustic frequency and Q_m as a function of trench depth. It can be seen that the main improvement that the trench brings in is to improve Q_m. A peak value of 323 is reached at the etch depth of 105 nm. This phenomenon can be explained by the node point theory [46]

What makes a difference here is the Q_m. As shown in Fig. 5 (c), compared to a typical slot waveguide (b=0), the additional etch depth improves the confinement of the acoustic mode. The mechanical Q factor of the selected acoustic mode reaches a peak value of 323 at the etch depth

of 105 nm. This phenomenon can be explained by the node point theory [46].

Fig. 6 (a), (b) and (c) show the mode distributions of selected modes at different etch depth. The acoustic wave distribution is slightly modified with the change of etch depth. As shown in Fig. 6 (d), a measured arc is placed on the side wall of the waveguide, the acoustic wave displacement on the arc is extracted. The collected data is shown in Fig. 6 (e). It can be seen that when the etch depth changes from 0 to 105 nm, the displacement at the interface between Si and AlN gradually decreases to zero (a node point), corresponding to the increase of the Q_m. After 105 nm, the displacement at the interface quickly goes to the opposite direction, leading to the leakage of the acoustic wave.

This is because at 105 nm, the acoustic mode distribution resembles the in-plane, out-of-phase fundamental mechanical mode of a tuning fork structure [47]. This form would enable the total force and moment at the outer end of the clamps to be zero, resulting in a lower anchor loss [48].

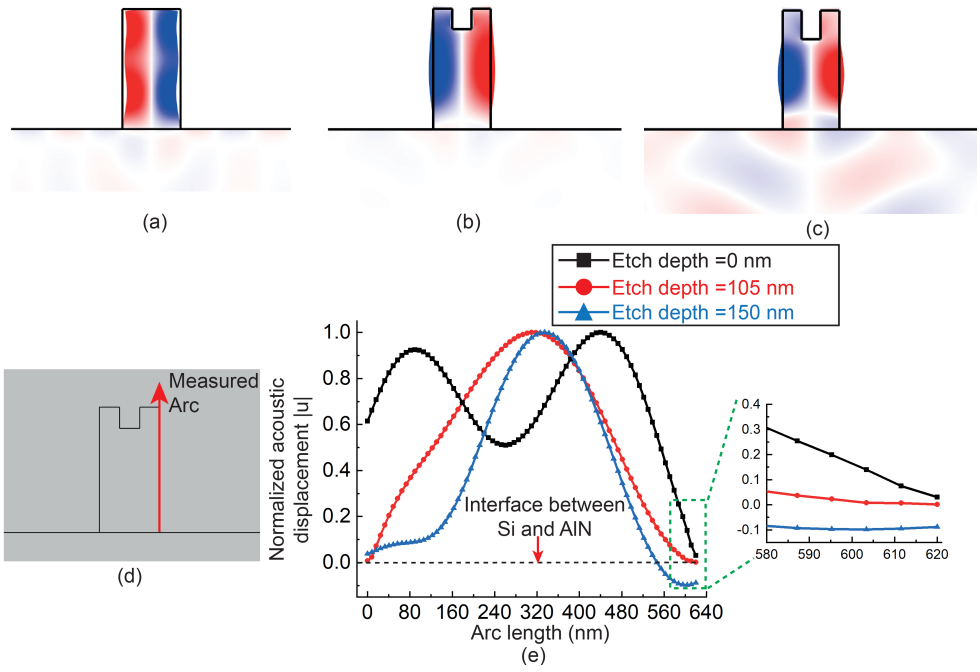

Fig. 6. The influence of etching depth on acoustic wave: (a)-(c) shows the acoustic displacement at etch depth b of 0 nm, 105 nm and 150 nm, respectively. The energy leaking into the substrate at 105 nm is minimum, corresponding to the peak of Q_m. (d) illustrates the set-up for analysing the node point at the interface between Si and AlN. A measured arc is placed on the side-wall of the waveguide. The displacement is collected along the measured arc. (e) shows the normalized acoustic displacement along the measured arc at different b. From the zoom-in inset figure, it can be seen that when b changes from 0 to 105, the displacement at the interface gradually decreases to zero, corresponding to the increase of the Q_m. After 105 nm, the displacement at the interface quickly goes to the other direction, leading to the leakage of the acoustic wave.

To provide a better understanding of what happens in the substrate, the authors also plot an absolute mechanical field on a logarithmic scale ($\log|u|$), which is shown in Fig. 7. It can be seen that at the optimized etch depth, the acoustic field leaked into the substrate is almost negligible, indicating the strong confinement of the acoustic mode. Meanwhile, the leakage at 150 nm etch depth is stronger than that of 0 nm etch depth. This matches with the results from Fig. 5 (c) that the Q_m at 150 nm is smaller than that at 0 nm.

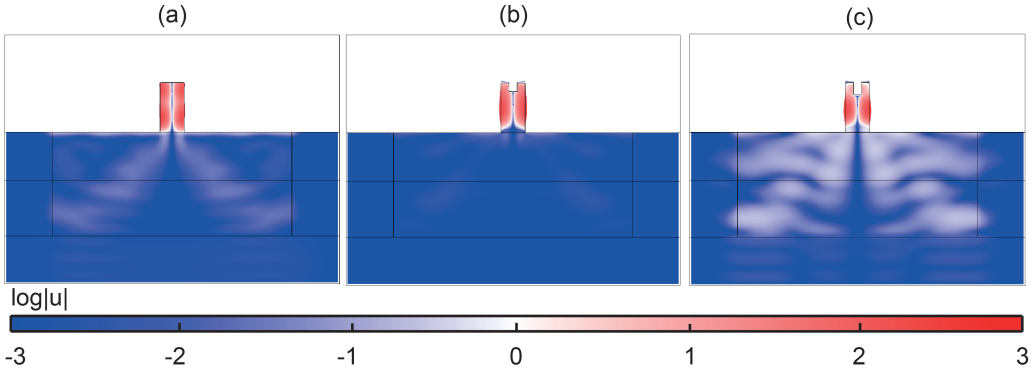

Fig. 7. The absolute mechanical mode distribution on on a logarithmic scale ($\log|u|$) at different etch depth: (a) to (c) corresponds to etch depth of 0 nm, 105 nm, 150 nm, respectively. At optimized etch depth, the acoustic field leaked into the substrate is almost negligible, indicating the strong confinement of the acoustic mode. Meanwhile, the leakage at 150 nm etch depth is stronger than that of 0 nm etch depth.

To conclude, at the optimized etch depth, the acoustic displacement at the interface of Si and AlN can be zero (a node point), leading to a reduced anchor loss and enhanced Q_m, thus enhanced total Brillouin gain coefficient.

The influence of the trench width on the final gain coefficient is also studied. The results are summarized in Fig. 8. Similar to the etch depth, there is a optimized Q_m with the change of trench width. However, the normalized gain coefficient g_0 is more sensitive to the change of trench width. g_0 will initially increase slightly and then rapidly decline after approximately 100 nm. This is because with the trench getting wider, the confinement of the optical mode is also getting weaker, leading to a decrease in both the photoelastic effect and moving boundary. A detailed analysis of the variation in the acoustic mode distribution when etch width changes is not shown here for the sake of simplicity but can be found in supplement 1 section 2.

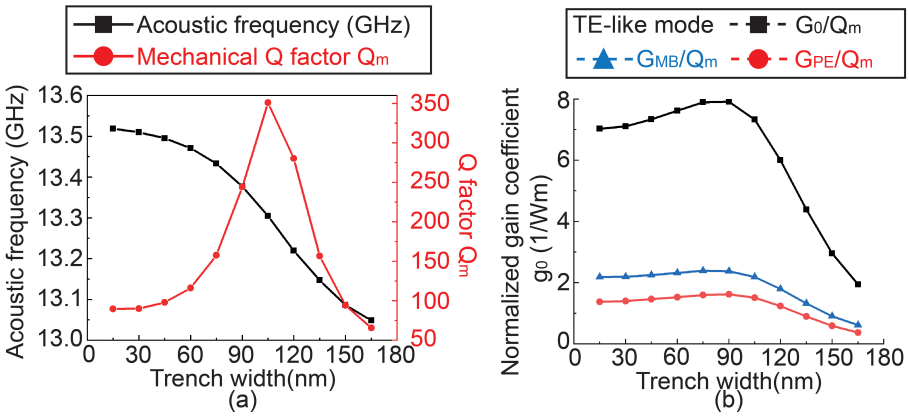

Fig. 8. The influence of etching width on the Brillouin gain coefficient: (a) is the acoustic frequency and Q_m as a function of trench width. With fixed trench depth, there is a matched trench width to achieve the maximum of Q_m. (b) shows the variation of normalized gain coefficient g_0 with the change of trench width. g_0 is more sensitive to the change of trench width than depth. It will first slightly increase and after around 100 nm it will quickly drop due to a weaker confinement of the optical mode.

3.3. Convergence progress of the GA for Optimized structure

In this project, the GA was run five times. Each time the initial population consists of different seeds. All the seeds are generated randomly, with the constraints that the structure is limited within the silicon layer and the maximum etching steps are two.We also focus on the fundamental optical modes of each generated structure.

For each run, the GA would arrive at slightly different results. This is due to the variation of the initial population and the uncontrolled crossover and mutation process during the optimization [49, 50]. However, each run would converge into a final SBS gain around 2000. The best result is what we reported in the Fig. 4 (a). Fig. 9 shows the convergence progress for the optimized structure. It converges into the optimized structure after 32 iterations.

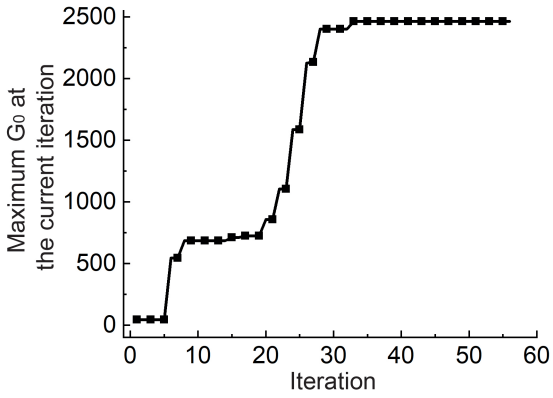

Fig. 9. The convergence progress for the optimized structure. It converges into the SBS gain around 2500 after 32 iterations.

4. Fabrication feasibility and tolerance analysis

Although the focus is on the theoretical analysis of Si-AlN-sapphire platform, here we introduce a promising fabrication route for realizing the opto-mechanical system that we propose.

To obtain the Si-AlN-Sapphire wafer, one can either deposit a silicon layer on the top of AlN [51] or direct wafer bond a device silicon layer with a commercial AlN-Sapphire wafer [52]. The deposition method benefits from higher efficiency and easier process [51], while direct wafer bonding has the advantages of better surface roughness and crystal quality [52], which will greatly affect the performance of SBS device [25]. Therefore, direct wafer bonding is preferred for this specific application.

Recently, a hydrophilic wafer bonding process is reported to further enhance the bonding quality between silicon and AlN layers [23]. The core procedure of the process is to activate the AlN layer with a plasma etching. This specific plasma, including O_2, Ar, SF_6, can change the chemical properties and topography of the AlN layer. After the plasma activation, AlN layer will have enhanced hydrophilicity, reduced surface roughness and low nanotopography. All of these changes lead to a strong and solid bonding between silicon and AlN layers [23]. Via this method, a strong bonding can be formed between the silicon and AlN layers, and both silicon and AlN can retain the crystalline quality of the pre-bonded wafers.

In this model, the silicon waveguide is aligned the <110> direction. In this way, higher photoelastic constants can be obtained to increase the final SBS gain coefficient [53]. During the mask design, the waveguide should be placed to align with the crystal orientation <110>.

To fabricate the structure, mature silicon photonic etching recipes can be applied [54]. Alignment between the two etching steps is important. Similar etching procedure has been demonstrated in a micro ring resonator with shallow-etched periodic grating on the top of the waveguide [55]. Fig. 10 shows the tolerance for the misalignment of the trench, it can be seen that if the trench is off centre by roughly 15 nm, the total gain coefficient will drop by half.

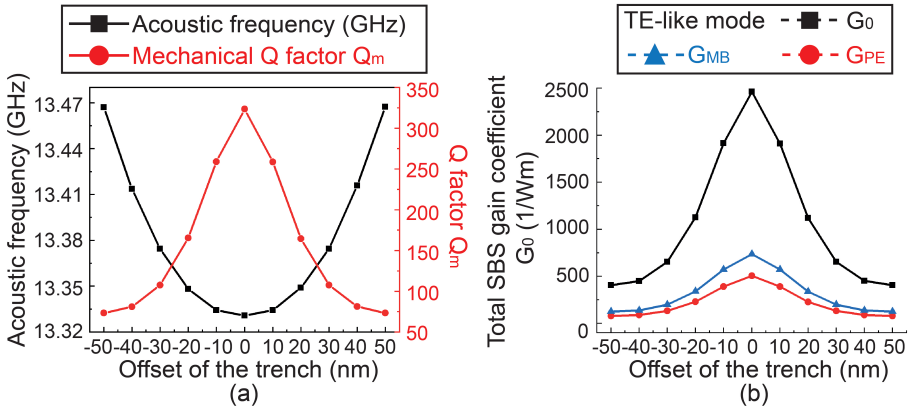

Fig. 10. The tolerance analysis of the offset of the trench: (a) shows the acoustic frequency and Q_m versus the offset of the trench. (b) shows the changes of the total Brillouin gain coefficient and two contributions when the trench shifts away from the centre. it can be seen that if the trench is off the centre by roughly 15 nm, the total gain coefficient will drop by half.

5. Conclusion

In this paper, we propose a novel Si-AlN-Sapphire platform for realizing a strong Brillouin scattering interaction without suspending the silicon core waveguide. This platform cannot only improve the mechanical and thermal stability, but can also simplify the fabrication difficulty without sacrificing the crystal quality of the platform.

We apply a full-vectorial formalism to calculate the Brillouin gain, including the photoelastic effect as well as the moving boundary contribution. To compensate for the reduction in the total gain coefficient in unsuspended structure due to the decreased moving boundary contribution, genetic algorithm is applied to optimize the waveguide structure and total gain coefficient. During the optimization, the maximum etching step is limited to two so that the final structure can be fabricable. A final structure with a shallow trench on the top of the silicon waveguide is found. This design can realize a total gain value of 2462 $W^{-1}m^{-1}$, which is 8 times larger than the recently reported result in unsuspended silicon waveguide. Further analysis found that the additional trench can create a node point at the interface between Si and AlN interface. This phenomenon will greatly suppress the anchor loss and can improve the Q_m to a level that limited by the fundamental material loss. We envisage that this system would be useful for the application in growing massive integrated photonic circuit [56] and on-chip signal processing [57].

Funding.
This work is supported by the Engineering and Physical Sciences Research Council (EPSRC EP/V000624/1)

Acknowledgments.
The authors acknowledge the use of the IRIDIS High Performance Computing Facility, and associated support services at the University of Southampton, in the completion of this work.

Disclosures.
Peng LI and Shumeng WANG contribute equally to this paper. The authors declare no conflicts of interest.

Data Availability Statement.
The data that support the findings of this study are openly available ay the University of Southampton ePrints research repository [58].

Supplemental document.
See Supplement 1 for supporting content.

References

1. R. W. Boyd, *Nonlinear optics* (Academic, 2020).
2. R. Chiao, C. Townes, and B. Stoicheff, "Stimulated Brillouin scattering and coherent generation of intense hypersonic waves," Phys. Rev. Lett. **12**, 592–595 (1964).
3. P. T. Rakich, C. Reinke, R. Camacho, P. Davids, and Z. Wang, "Giant enhancement of stimulated Brillouin scattering in the subwavelength limit," Phys. Rev. X **2**, 011008 (2012).
4. R. Pant, C. G. Poulton, D.-Y. Choi, H. Mcfarlane, S. Hile, E. Li, L. Thevenaz, B. Luther-Davies, S. J. Madden, and B. J. Eggleton, "On-chip stimulated Brillouin scattering," Opt. express **19**, 8285–8290 (2011).
5. B. Morrison, A. Casas-Bedoya, G. Ren, K. Vu, Y. Liu, A. Zarifi, T. G. Nguyen, D.-Y. Choi, D. Marpaung, A. M. Madden, Stephen J, and B. J. Eggleton, "Compact Brillouin devices through hybrid integration on silicon," Optica **4**, 847–854 (2017).
6. R. Van Laer, B. Kuyken, D. Van Thourhout, and R. Baets, "Interaction between light and highly confined hypersound in a silicon photonic nanowire," Nat. Photonics **9**, 199–203 (2015).
7. R. Van Laer, A. Bazin, B. Kuyken, R. Baets, and D. Van Thourhout, "Net on-chip Brillouin gain based on suspended silicon nanowires," New J. Phys. **17**, 115005 (2015).
8. E. A. Kittlaus, N. T. Otterstrom, and P. T. Rakich, "On-chip inter-modal Brillouin scattering," Nat. communications **8**, 1–9 (2017).
9. F. Gyger, J. Liu, F. Yang, J. He, A. S. Raja, R. N. Wang, S. A. Bhave, T. J. Kippenberg, and L. Thévenaz, "Observation of stimulated Brillouin scattering in silicon nitride integrated waveguides," Phys. review letters **124**, 013902 (2020).
10. K. Wang, J. Sun, and M. Cheng, "Design of partially suspended silicon nitride slot waveguides for efficient forward stimulated Brillouin scattering," IEEE Photonics J. **12**, 1–11 (2020).
11. W. Jin, L. Chang, W. Xie, H. Shu, J. D. Peters, X. Wang, and J. E. Bowers, "Stimulated Brillouin scattering in AlGaAs on insulator waveguides," in *CLEO: Science and Innovations,* (Optical Society of America, 2020), pp. SM4–L7.
12. J. Song, X. Guo, W. Peng, J. Pan, L. Wan, T. Feng, S. Zeng, D. Liu, B. Zhang, M. Zhang, and Z. Li, "Stimulated Brillouin scattering in low-loss Ge25Sb10S65 chalcogenide waveguides," J. Light. Technol. **39**, 5048–5053 (2021).
13. D. Thomson, A. Zilkie, J. E. Bowers, T. Komljenovic, G. T. Reed, L. Vivien, D. Marris-Morini, E. Cassan, L. Virot, J.-M. Fédéli, J.-M. Hartmann, J. H. Schmid, D.-X. Xu, F. Boeuf, P. O'Brien, G. Z. Mashanovich, and M. Nedeljkovic, "Roadmap on silicon photonics," J. Opt. **18**, 073003 (2016).
14. W. Qiu, P. T. Rakich, H. Shin, H. Dong, M. Soljačić, and Z. Wang, "Stimulated Brillouin scattering in nanoscale silicon step-index waveguides: a general framework of selection rules and calculating SBS gain," Opt. express **21**, 31402–31419 (2013).
15. M. K. Schmidt, C. G. Poulton, G. Z. Mashanovich, G. T. Reed, B. J. Eggleton, and M. Steel, "Suspended mid-infrared waveguides for Stimulated Brillouin Scattering," Opt. Express **27**, 4976–4989 (2019).
16. L. Mercadé, A. V. Korovin, Y. Pennec, J. Ahopelto, B. Djafari-Rouhani, and A. Martínez, "Vertical engineering for large Brillouin gain in unreleased silicon-based waveguides," Phys. Rev. Appl. **15**, 034021 (2021).
17. X. Meng, Y.-C. Byun, H. S. Kim, J. S. Lee, A. T. Lucero, L. Cheng, and J. Kim, "Atomic layer deposition of silicon nitride thin films: a review of recent progress, challenges, and outlooks," Materials **9**, 1007 (2016).
18. Q. Fan, C. Chai, Q. Wei, P. Zhou, and Y. Yang, "Elastic anisotropy and electronic properties of Si3N4 under pressures," AIP Adv. **6**, 085207 (2016).
19. P. Li, J.-Y. Ou, G. Z. Mashanovich, and J. Yan, "Tailorable stimulated Brillouin scattering in a partially suspended aluminium nitride waveguide in the visible range," Opt. Express **30**, 27092–27108 (2022).
20. J. Pastrňák and L. Roskovcová, "Refraction index measurements on AlN single crystals," physica status solidi (b) **14**, 5–8 (1966).
21. A. Wright, "Elastic properties of zinc-blende and wurtzite AlN, GaN, and InN," J. Appl. physics **82**, 2833–2839 (1997).
22. B. J. Eggleton, C. G. Poulton, and R. Pant, "Inducing and harnessing stimulated Brillouin scattering in photonic integrated circuits," Adv. Opt. Photonics **5**, 536–587 (2013).
23. J. Kaaos, G. Ross, and M. Paulasto-Krockel, "Aluminum Nitride to silicon direct bonding for an alternative Silicon-On-Insulator platform," ACS applied materials & interfaces **13**, 38857–38865 (2021).
24. C. Wolff, M. J. Steel, B. J. Eggleton, and C. G. Poulton, "Stimulated Brillouin scattering in integrated photonic waveguides: Forces, scattering mechanisms, and coupled-mode analysis," Phys. Rev. A **92**, 013836 (2015).
25. C. Wolff, R. Soref, C. Poulton, and B. Eggleton, "Germanium as a material for stimulated Brillouin scattering in the mid-infrared," Opt. express **22**, 30735–30747 (2014).
26. J. Håkansson and D. Van Thourhout, "Generating novel waveguides for stimulated Brillouin scattering with genetic algorithms," APL Photonics **4**, 010803 (2019).

27. C. Wolff, M. Steel, and C. Poulton, "Formal selection rules for Brillouin scattering in integrated waveguides and structured fibers," Opt. express **22**, 32489–32501 (2014).
28. R. N. Candler, H. Li, M. Lutz, W.-T. Park, A. Partridge, G. Yama, and T. W. Kenny, "Investigation of energy loss mechanisms in micromechanical resonators," in *TRANSDUCERS'03. 12th International Conference on Solid-State Sensors, Actuators and Microsystems. Digest of Technical Papers,* vol. 1 (IEEE, 2003), pp. 332–335.
29. J. E.-Y. Lee, J. Yan, and A. A. Seshia, "Anchor limited Q in flexural mode resonators," in *2008 IEEE Ultrasonics Symposium,* (IEEE, 2008), pp. 2213–2216.
30. J. Lee, J. Yan, and A. Seshia, "Quality factor enhancement of bulk acoustic mode resonators through anchor geometry design," Proc. EUROSENSORS XXII (2008).
31. J. E. Lee, J. Yan, and A. A. Seshia, "Study of lateral mode SOI-MEMS resonators for reduced anchor loss," J. Micromechanics Microengineering **21**, 045010 (2011).
32. H. Li, "Refractive index of silicon and germanium and its wavelength and temperature derivatives," J. Phys. Chem. Ref. Data **9**, 561–658 (1980).
33. I. H. Malitson and M. J. Dodge, "Refractive-index and birefringence of synthetic sapphire," in *Journal Of The Optical Society Of America,* vol. 62 (AMER INST PHYSICS CIRCULATION FULFILLMENT DIV, 1972), pp. 1405–1405.
34. J. Wortman and R. Evans, "Young's modulus, shear modulus, and poisson's ratio in silicon and germanium," J. applied physics **36**, 153–156 (1965).
35. J. Winey, Y. Gupta, and D. Hare, "R-axis sound speed and elastic properties of sapphire single crystals," J. Appl. Phys. **90**, 3109–3111 (2001).
36. D. K. Biegelsen, "Photoelastic tensor of silicon and the volume dependence of the average gap," Phys. Rev. Lett. **32**, 1196 (1974).
37. S. Y. Davydov, "Evaluation of physical parameters for the group III nitrates: BN, AlN, GaN, and InN," Semiconductors **36**, 41–44 (2002).
38. F. De Leonardis, R. A. Soref, M. Soltani, and V. M. Passaro, "Stimulated Brillouin scattering in an AlGaN photonics platform operating in the visible spectral range," Sci. reports **8**, 1–13 (2018).
39. B. Helme and P. King, "The phonon viscosity tensor of Si, Ge, GaAs, and InSb," physica status solidi (a) **45**, K33–K37 (1978).
40. B. A. Auld, "Chapter 3 - Elastic properties of solids," in *Acoustic fields and waves in solids,* vol. 1 (Wiley, 1992), pp. 75–78.
41. A. Frangi, A. Bugada, M. Martello, and P. Savadkoohi, "Validation of PML-based models for the evaluation of anchor dissipation in MEMS resonators," Eur. J. Mech. **37**, 256–265 (2013).
42. D. M. Mukhopadhyay, M. O. Balitanas, A. Farkhod, S.-H. Jeon, and D. Bhattacharyya, "Genetic algorithm: A tutorial review," Int. journal grid distributed computing **2**, 25–32 (2009).
43. A. Hassanat, K. Almohammadi, E. Alkafaween, E. Abunawas, A. Hammouri, and V. S. Prasath, "Choosing mutation and crossover ratios for genetic algorithms—a review with a new dynamic approach," Information **10**, 390 (2019).
44. H. Wu, K. Zhang, C. He, L. He, Q. Wang, W. Zhao, and Z. Chen, "Recent advances in fabricating Wurtzite AlN Film on (0001)-Plane Sapphire substrate," Crystals **12**, 38 (2021).
45. P. Li, J.-Y. Ou, and J. Yan, "Method for optimising the performance of PML in anchor-loss limited model via COMSOL," IET Sci. Meas. & Technol. (2022).
46. S. Humad, R. Abdolvand, G. K. Ho, G. Piazza, and F. Ayazi, "High frequency micromechanical piezo-on-silicon block resonators," in *IEEE International Electron Devices Meeting 2003,* (IEEE, 2003), pp. 39–42.
47. V. Zega, A. Frangi, A. Guercilena, and G. Gattere, "Analysis of frequency stability and thermoelastic effects for slotted tuning fork MEMS resonators," Sensors **18**, 2157 (2018).
48. R. Zhang, C. Ti, M. I. Davanco, Y. Ren, V. Aksyuk, Y. Liu, and K. Srinivasan, "Integrated tuning fork nanocavity optomechanical transducers with high f MQM product and stress-engineered frequency tuning," Appl. Phys. Lett. **107**, 131110 (2015).
49. J. Huang, H. Ma, D. Chen, H. Yuan, J. Zhang, Z. Li, J. Han, J. Wu, and J. Yang, "Digital nanophotonics: The highway to the integration of subwavelength-scale photonics: Ultra-compact, multi-function nanophotonic design based on computational inverse design," Nanophotonics **10**, 1011–1030 (2020).
50. Y. Meng, Y. Chen, L. Lu, Y. Ding, A. Cusano, J. A. Fan, Q. Hu, K. Wang, Z. Xie, Z. Liu, Y. Yang, Q. Liu, M. Gond, Q. Xiao, S. Sun, M. Zhang, X. Yuan, and X. Ni, "Optical meta-waveguides for integrated photonics and beyond," Light. Sci. & Appl. **10**, 235 (2021).
51. M. F. Bhopal, D. Lee, A. u. Rehman, and S. H. Lee, "High temperature crystallization process of a-Si thin-films on aluminum nitride substrates," Silicon **10**, 171–175 (2018).
52. C. Men and C. Lin, "Characterization of bonded silicon-on-aluminum-nitride wafers with RBS, TEM and HRXRD techniques," Microelectron. engineering **85**, 1807–1810 (2008).
53. K. Gomi and Y. Niitsu, "Effect of crystalline orientation on photoelastic constant of Si single crystal," in *International Symposium on Polarization Analysis and Applications to Device Technology,* vol. 2873 (SPIE, 1996), pp. 238–241.
54. B. Wu, A. Kumar, and S. Pamarthy, "High aspect ratio silicon etch: A review," J. applied physics **108**, 9 (2010).
55. Z. Shao, J. Zhu, Y. Zhang, Y. Chen, and S. Yu, "On-chip switchable radially and azimuthally polarized vortex beam generation," Opt. Lett. **43**, 1263–1266 (2018).
56. M. Merklein, A. Casas-Bedoya, D. Marpaung, T. F. Büttner, M. Pagani, B. Morrison, I. V. Kabakova, and B. J. Eggleton, "Stimulated Brillouin scattering in photonic integrated circuits: novel applications and devices," IEEE J.

Sel. Top. Quantum Electron. **22**, 336–346 (2016).
57. A. Choudhary, Y. Liu, D. Marpaung, and B. J. Eggleton, "On-chip Brillouin filtering of RF and optical signals," IEEE journal selected topics quantum electronics **24**, 1–11 (2018).
58. P. Li, "ResearchData:EnhancedSBS," https://doi.org/10.5258/SOTON/D2513.